Energy & Environmental Science

ROYAL SOCIETY OF CHEMISTRY

PAPER

View Article Online
View Journal | View Issue

Cite this: *Energy Environ. Sci.*, 2025, **18**, 9590

Rigid–flexible synergized polymer dielectrics with multiple crosslinking networks for high-temperature electrostatic energy storage

Baotieliang Wang,†[ac] Jichun Zhao,†[ac] Chuanjia Jiao,[ac] Jiayan Li,[ac] Zhaoyu Ran,[b] Donghua Xu,[a] Zhaoyan Sun,*[ac] Qi Li,*[b] Jiawei Zou*[a] and Shifang Luan*[ac]

High-temperature dielectric energy storage materials are essential for next-generation power electronics and electrical systems operating in extreme environments. However, achieving high-energy storage in polymer dielectrics at ultrahigh temperatures (*e.g.*, 200 °C) remains a critical challenge, chiefly owing to the marked enhancement of molecular chain thermal motion, which gives rise to elevated charge conduction losses and diminished breakdown strength. Here, we propose a rigid–flexible synergistic multiple crosslinked network strategy that simultaneously suppresses inter/intra-chain charge transport while inhibiting thermal molecular motion. This rigid crosslinked architecture supports adjacent polymer chains, enhancing local segmental stability while also reducing interchain π–π stacking and dipole interactions. Furthermore, enabled by the thermodynamic annealing of flexible segments, the homogenously distributed interchain rigid scaffolds strike a balance between local structural rigidity and global deformability, thereby efficiently mitigating bulk charge conduction and boosting energy storage capabilities under extreme conditions. The resulting material exhibits an exceptional energy storage performance at 200 °C, with a discharge energy density of 6.91 J cm^{-3} at 90% efficiency. Moreover, it demonstrates outstanding cycling stability, maintaining high performance with over 50 000 charge–discharge cycles at 500 MV m^{-1}. This study presents a new design strategy for high-temperature dielectric materials, showcasing the potential of multiple crosslinked structures to meet the demanding requirements of ultrahigh-temperature applications.

Received 16th July 2025,
Accepted 25th September 2025

DOI: 10.1039/d5ee04064g

rsc.li/ees

Broader context

High-temperature dielectric energy storage demands materials that resist performance degradation from molecular chain thermal motion and interchain interactions, which exacerbate charge conduction. Existing crosslinking strategies improve thermal stability but fail to effectively suppress molecular vibration and interchain interactions (*e.g.*, π–π stacking and dipole coupling), limiting high-temperature energy storage. Herein, we propose a rigid–flexible synergistic multiple crosslinked network design: rigid crosslinking scaffolds constrain chain motion and reduce interchain interactions, while flexible segments enable thermodynamic stability and mitigate stress concentration. This strategy simultaneously suppresses inter/intra-chain charge transport, achieving 6.91 J cm^{-3} at 90% efficiency at 200 °C with robust cycling stability.

1. Introduction

The advancement of microelectronics and electrical systems has raised significant requirements for electrostatic energy storage dielectric polymer materials, particularly for maintaining high discharge energy density and charge–discharge efficiency across a wide temperature range.[1–6] For instance, silicon-based electronic components operate at temperatures up to 150 °C,[7] while the internal electronic control systems of electric vehicles utilizing semiconductor power electronics can reach temperatures as high as 200 °C.[8] However, currently available commercial biaxially oriented polypropylene (BOPP) capacitors have a working temperature limit of only 105 °C. At higher temperatures, enhanced molecular thermal motion results in a marked decline in the insulation and capacitive performances of these materials. Although commercial high

[a] *State Key Laboratory of Polymer Science and Technology, Changchun Institute of Applied Chemistry, Chinese Academy of Sciences, Changchun 130022, China. E-mail: zysun@ciac.ac.cn, jwzou@ciac.ac.cn, sfluan@ciac.ac.cn*
[b] *State Key Laboratory of Power System, Department of Electrical Engineering, Tsinghua University, Beijing 100084, China. E-mail: qili1020@tsinghua.edu.cn*
[c] *School of Applied Chemistry and Engineering, University of Science and Technology of China, Hefei 230026, China*
† Equal contribution.

glass transition temperature (T_g) polymers exhibit improved thermal stability, their substantial energy losses at elevated temperatures restrict practical applications. For instance, PI-Kapton (T_g > 350 °C) demonstrates an energy density of 1.2 J cm^{-3} and an efficiency of only 60% at 150 °C. The currently available commercial polymeric dielectric films, regardless of standard or high-temperature designs, struggle to provide high energy density under high-temperature conditions. This necessitates the addition of cooling devices to ensure the stable operation of capacitors in high-temperature environments, such as in electric drive transportation, thereby increasing equipment size and costs. Therefore, it is imperative to develop dielectric materials with high energy density that can withstand the harsh conditions at 200 °C, not only to meet the demands of extreme applications but also to enhance device stability.

At lower temperatures, charge transport in polymers is dominated by Ohmic conduction, with electrode/dielectric interface injection emerging as a gradual contributing factor to conductivity as temperature rises.[9,10] In ultrahigh-temperature regimes (above 200 °C), enhanced molecular chain mobility and elevated energy states of charge carriers/impurity ions enable thermal activation, allowing carriers to overcome energy barriers or facilitate bulk conduction *via* tunneling effects.[11,12] Recent studies have demonstrated that pronounced interchain interactions in polymers at elevated temperatures enhance bulk charge carrier transport, as exemplified by phonon-assisted interchain carrier transfer induced by transverse molecular chain vibrations,[13] strengthened interchain charge transfer through π–π stacking,[14] and increased high-temperature conduction losses resulting from interchain dipole coupling.[15] Therefore, suppressing the thermal motion of the chains and reducing interchain interactions is critical for maintaining high bulk insulation performance. Crosslinking of dielectric polymers represents an effective strategy for enhancing high-temperature insulation, as it not only reduces segmental relaxation but also introduces charge carrier traps. Yu *et al.* constructed a crosslinked structure through coulombic and hydrogen bonding interactions,[10] Shen *et al.* established physical crosslinking *via* electrostatic interactions,[16] and Wang *et al.* developed a rigid crosslinked network based on maleic anhydride,[17] all exhibiting excellent energy storage performance at elevated temperatures. However, current crosslinking strategies still lack exploration into the suppression of interchain interactions. Effectively and stably mitigating interchain interactions through the design of a polymer structure remains a significant challenge.

In response to these challenges, we have developed a rigid–flexible synergistic multiple crosslinked network architecture with significant improvements that effectively suppresses both interchain and intrachain charge transport while concurrently restricting thermally induced molecular motion. This large-sized rigid crosslinked architecture supports adjacent polymer chains, enhancing local segmental stability while also reducing interchain π–π stacking and dipole interactions. Furthermore, the incorporation of flexible alkyl chain structures balances the rigidity of the fully crosslinked polymer system, thereby mitigating localized charge/stress concentration, and disrupting intrachain conjugation. This multi-component synergistic polymer structure exhibits lower electrical conduction losses and higher breakdown strength compared to single-component polymers. At 200 °C, it attains an exceptionally high energy density of 6.91 J cm^{-3} at an efficiency of 90% and maintains decent stability after 50 000 cycles under a high electric field of 500 MV m^{-1}. The multiple crosslinking structure proposed herein offers a novel solution to inhibit charge carrier transport at ultra-high temperatures and enhance energy storage performance.

2. Results and discussion

2.1. Molecular structural of multiple polyimides

To construct a multi-crosslinked polyimide with a rigid–flexible structure, three different functional diamine monomers were predominantly employed through copolymerization, while the anhydride structure was 4,4′-hexafluoroisopropylene dianhydride (6FDA). The functional monomers utilized in the material included a phenolphthalein diamine that provides large-sized rigid crosslinking, an alkyl diamine that offers a flexible main chain, and a cyanoethyl benzoate diamine that serves as the fundamental unit for establishing a normal crosslinking network (Fig. 1a). Following thermal treatment, the lactone rings in the phenolphthalein structure and the benzoate moieties in the cyanoethyl benzoate diamine decompose into free radicals, thereby forming an inter-chain crosslinked structure (Fig. S1). In this work, several polyimide structures were designed, among which the most fundamental structure, completely devoid of functional groups and crosslinking moieties, was designated as C0, representing the product of the homopolymerization of *m*-phenylenediamine and 6FDA. The structure containing 10% phenolphthalein component and 90% cyanoethyl benzoate was termed PC, characterized by a high crosslinking density and superior rigidity. Meanwhile, the structure comprising 10% phenolphthalein diamine, 10% aliphatic diamine, and 80% cyanoethyl benzoate was referred to as PAC. Fig. S2 illustrates the scheme of the cross-linking reaction for the polymer comprising phenolphthalein diamine and cyanoethyl benzoate. The molecular structures were confirmed using ^{1}H-NMR (Fig. S3–S12) and ATR-FTIR (Fig. S13). The molecular weights were characterized through GPC (Fig. S14). The thermal stability of the polymers was analyzed using TGA (Fig. S15) and DSC (Fig. S16).

2.2. Structural characterization of rigid crosslinked and rigid–flexible synergistic networks

The introduction of large-sized rigid crosslinking structures into polymer crosslinking networks aims to enhance interchain support, thereby alleviating the carrier transport issues arising from longitudinal chain vibrations, π–π interactions and dipole interactions under extreme conditions and high electric fields. On this basis, flexible alkyl segments with higher degrees of freedom in chain motion were incorporated to balance the distribution of molecular chains and reduce the distortions and thermodynamically unstable stacking of molecular chains

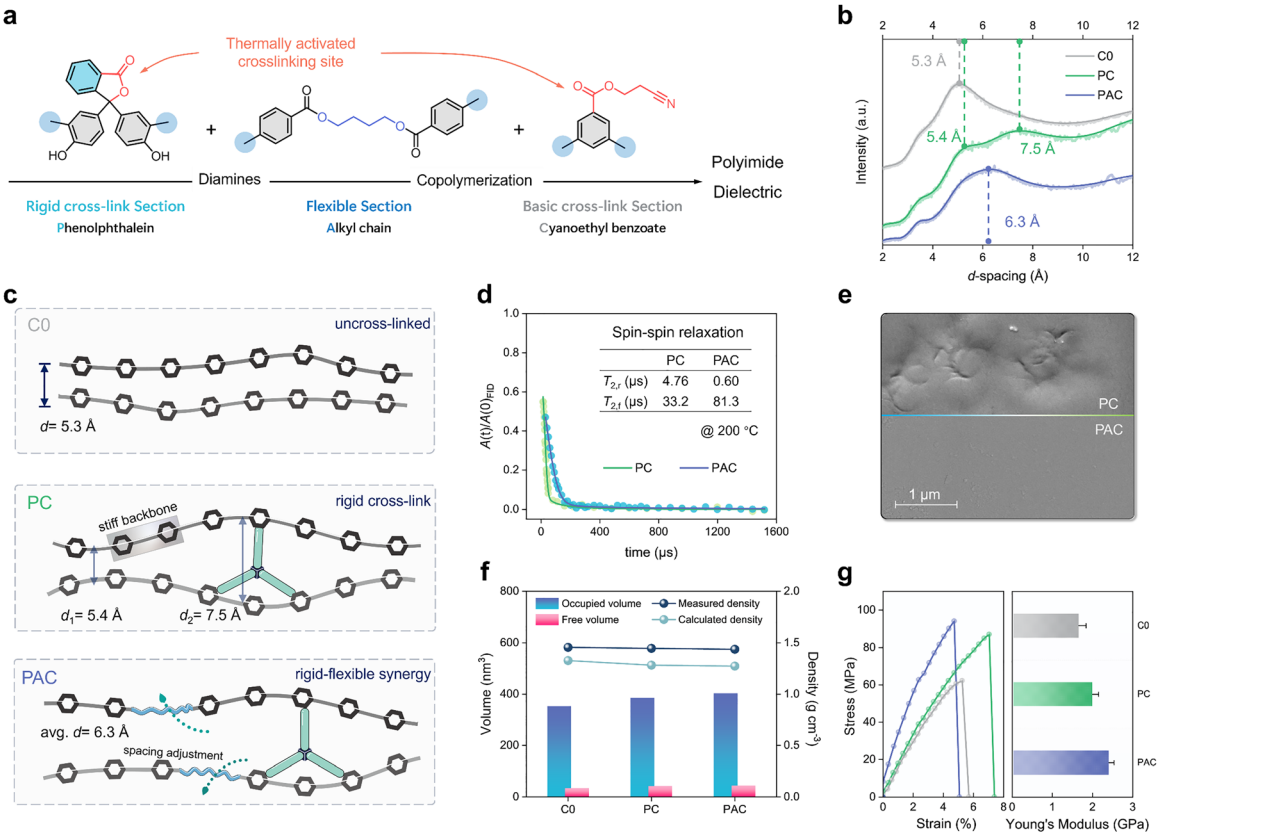

Fig. 1 Multiple structural characterization of rigid–flexible synergistic polymer networks. (a) Structures of functional diamines. (b) Molecular chain distribution of C0, PC, and PAC derived from wide-angle X-ray diffraction and the (c) corresponding chain conformation schematic diagram. (d) Spin–spin relaxation time (T_2) measured by low-field solid-state nuclear magnetic resonance. (e) Micrometer-scale polymer surface morphology characterized by scanning electron microscopy. (f) Occupied volume, free volume, measured density and calculated density of C0, PC and PAC. (g) Strain–stress curves and Young's modulus of C0, PC and PAC.

caused by excessive rigidity, as well as inhibit intrachain conjugation caused by aromatic rings.

We conducted a comprehensive characterization of the crosslinked polymers across multiple scales, from the microscopic to the mesoscopic level. The structures below 1 nm are often characterized by wide-angle X-ray diffraction[18] (WAXD, Fig. S17), through which the average distance between molecular chains can be determined by analyzing the amorphous peaks. According to the *d*-spacing distribution curves presented in Fig. 1b, the molecular chains of C0 demonstrate a uniform distribution characterized by a *d*-spacing of 5.3 Å. In contrast, the fully crosslinked polymer PC, which incorporates large-sized rigid phenolphthalein as the crosslinker, reveals two distinct broad peaks with average *d*-spacing values of 5.4 Å and 7.5 Å, with the latter peak exhibiting a notably higher intensity. This new spacing is attributed to the phenolphthalein crosslinks serving as rigid molecular scaffolds, thereby generating substantial steric hindrance that enlarges the interchain distance. However, due to the rigidity of the polyimide backbone, this supporting effect is insufficient to influence the configurational changes of the main chain through internal stresses, thus failing to alter the interchain spacing of unlinked segments. Based on this, PAC contains both rigid crosslinks and flexible alkyl main chain segments, and the deformable alkyl chains effectively dissipate the internal stresses caused by the rigid crosslinks and adjust the uneven distribution of molecular chains. Consequently, PAC exhibits a single broad peak in the *d*-spacing curves at approximately 6.3 Å, in contrast to the distinct structure observed in PC. Fig. 1c illustrates the schematic representation of the molecular chain distribution structures of C0, PC and PAC.

The distinct differences in molecular chain distribution between the rigid-crosslinked-only PC and the rigid–flexible synergistic PAC motivate further investigation into the molecular chain dynamic freedom in these structures using low-field solid-state nuclear magnetic resonance (LF-NMR). Fig. 1d and Fig. S18 show the fitting results of free induction decay and Hahn echo for PC and PAC. Given the presence of crosslinked restricted segments and uncrosslinked free segments in the crosslinked polymers, the corresponding data were fitted using a two component Weibull distribution to characterize the motion states of crosslinked and uncrosslinked segments,[19] described by the following equation:

$$f(t) = A(\exp(-(t/T_2)^a) + \exp(-(t/T_2)^b))$$

where A is the amplitude, and T_2 is the spin–spin relaxation time (a shorter T_2 implies more restricted segmental motion[20]), and a and b are shape parameters. At 200 °C, PC exhibits free-state relaxation time ($T_{2,f}$) and restricted-state relaxation time

($T_{2,r}$) of 33.2 μs and 4.76 μs, respectively, whereas PAC shows $T_{2,f}$ of 81.3 μs and $T_{2,r}$ of 0.60 μs. These results indicate that the free-state segments (including flexible main chains) in PAC have higher mobility than those in PC, while the restricted-state segments (rigid crosslinked) in PAC are more constrained. The introduction of alkyl chain enhances the backbone mobility, which facilitates the balancing of molecular chain distribution and the release of internal stress. In contrast, the single rigid structure in PC restricts chain motion, leading to uneven distribution and stacking of crosslinking sites that trap rigid crosslinked points in a metastable state, hence the longer relaxation time (4.76 μs). By comparison, the uniform crosslinking distribution and internal stress dissipation mediated by flexible chains in PAC stabilize the rigid crosslinked points, fully exerting their restrictive effect on molecular chain motion.

Utilizing small-angle X-ray scattering (SAXS), we investigated the larger-scale polymer chain structures. The results indicate that PC exhibits the highest scattering intensity in the scattering vector range of 0.08–0.15 nm^{-1}, suggesting that PC possesses the highest periodic structure content at this scale, corresponding to a size of approximately 42–78 nm, while the scattering vector of PAC is similar to that of non-rigid crosslinked polyimides (Fig. S19).

After demonstrating the effects of rigid cross-linking and flexible alkyl chains on the molecular chain structure of polymers, we employed a scanning electron microscope (SEM) to investigate their surface morphology for a more intuitive analysis of the changes, as shown in Fig. 1e and Fig. S20. PC films displayed numerous micron-sized scar structures, likely resulting from the excessive rigidity of phenolphthalein, which greatly hindered the mobility of the polymer segments during solution casting and cross-linking, leading to the unique surface morphology. In contrast, due to the flexible main chain's ability to modulate the molecular chains, PAC exhibits a smooth and uniform surface.

Molecular dynamics simulations[21,22] were employed to investigate the molecular chain packing of C0, PC, and PAC (Fig. S21), with comparative results shown in Fig. 1f. The non-crosslinked C0 demonstrates tightly packed molecular chains, yielding the smallest occupied volume (352 nm^3) and free volume (33 nm^3). In PC, the incorporated rigid structures impose spatial constraints that disrupt chain packing, resulting in increased occupied (384 nm^3) and free volumes (41 nm^3). This expansion suggests stabilized molecular conformations with enhanced intermolecular spacing. PAC introduces a flexible alkyl backbone that promotes chain mobility through entropy-driven diffusion, enabling greater volumetric occupation (401 nm^3) while preserving comparable free volume (43 nm^3) to PC. The free volume fraction progression (C0 < PC ≈ PAC) inversely mirrors the material density trend (C0 > PC ≥ PAC) observed in both theoretical calculations and experimental measurements data, with the agreement in density further validating the reliability of the simulated free volume fractions.

The XPS C1s spectra of C0, PC, and PAC show a progressive increase in C–C bond proportions by the incorporation of crosslinking and alkyl backbone (Fig. S22). PAC exhibits the narrowest C1s peak (FWHM = 1.18), indicating reduced chemical state dispersion,[23,24] which is likely attributed to the entropy-driven self-organization of flexible chains in PAC. This organization optimizes molecular chain distribution and mitigates local structural distortions induced by rigid crosslinks.

Mechanical characterization reveals a graded enhancement in the Young's modulus across C0, PC, and PAC (Fig. 1g). The linear densely packed C0 exhibits the lowest modulus of 1.65 GPa, PC constructs a chemically bonded network that restricts chain mobility, elevating the modulus to 1.99 GPa. However, PC's modulus remains inferior to fully short-chain crosslinked systems (2.50 GPa, Fig. S23), indicating that while rigid crosslinks enhance stiffness, their topological defects such as uneven chain distribution and expanded interchain spacing weaken intermolecular interactions, thereby compromising mechanical performance. PAC achieves a modulus of 2.40 GPa through entropy-driven conformational adjustments of flexible chains that homogenize crosslink distribution, demonstrating that rigid-flexible synergy effectively reconciles the conflict between crosslink density and structural defects.

2.3. Experimental investigations of carrier transport suppression in crosslinked polymer systems

Polymer dielectrics under elevated temperatures are often plagued by significant leakage currents, primarily originating from bulk conduction phenomena, including hopping conduction, Poole–Frenkel emission, and phonon-assisted interchain carrier migration. These mechanisms collectively degrade the material's resistivity and energy storage efficiency, posing critical challenges for high-temperature applications.

Fig. 2a presents the transition density matrix (TDM) simulations[25] to elucidate the suppression effect of rigid crosslinked networks on interchain carrier transport. The energy barriers for interchain electronic transitions from the ground state to the first ten excited states were compared between two crosslinking structures: phenolphthalein cyanobenzoate (P–C) and cyanobenzoate homocrosslinking (C–C). This comparison is motivated by the dominance of P–C crosslinks in PC and PAC systems, where the theoretical P–C/P–P ratios are 18 : 1 and 16 : 1, respectively. The rigid phenolphthalein moieties in P–C crosslinks introduce steric hindrance, and concurrently constrain chain conformational flipping and motion, which increases interchain spacing and reduces π–π stacking between aromatic rings. Consequently, the total interchain electronic excitation energy for P–C crosslinks (12.57 a.u.) is approximately one-fifth of that for C–C crosslinks (59.52 a.u.), demonstrating the critical role of rigid crosslinkers in suppressing carrier delocalization.

On the other hand, the rigid polyaromatic structure may facilitate intrachain carrier transport due to extended π-electron delocalization, whereas incorporating alkyl main chains can suppress carrier migration along the molecular backbone by disrupting conjugation continuity. As shown in Fig. 2b, the excited-state energy levels for intrachain carrier transport were calculated at the terminal positions of P, C, and A units. The P unit exhibits the lowest energy barrier, followed

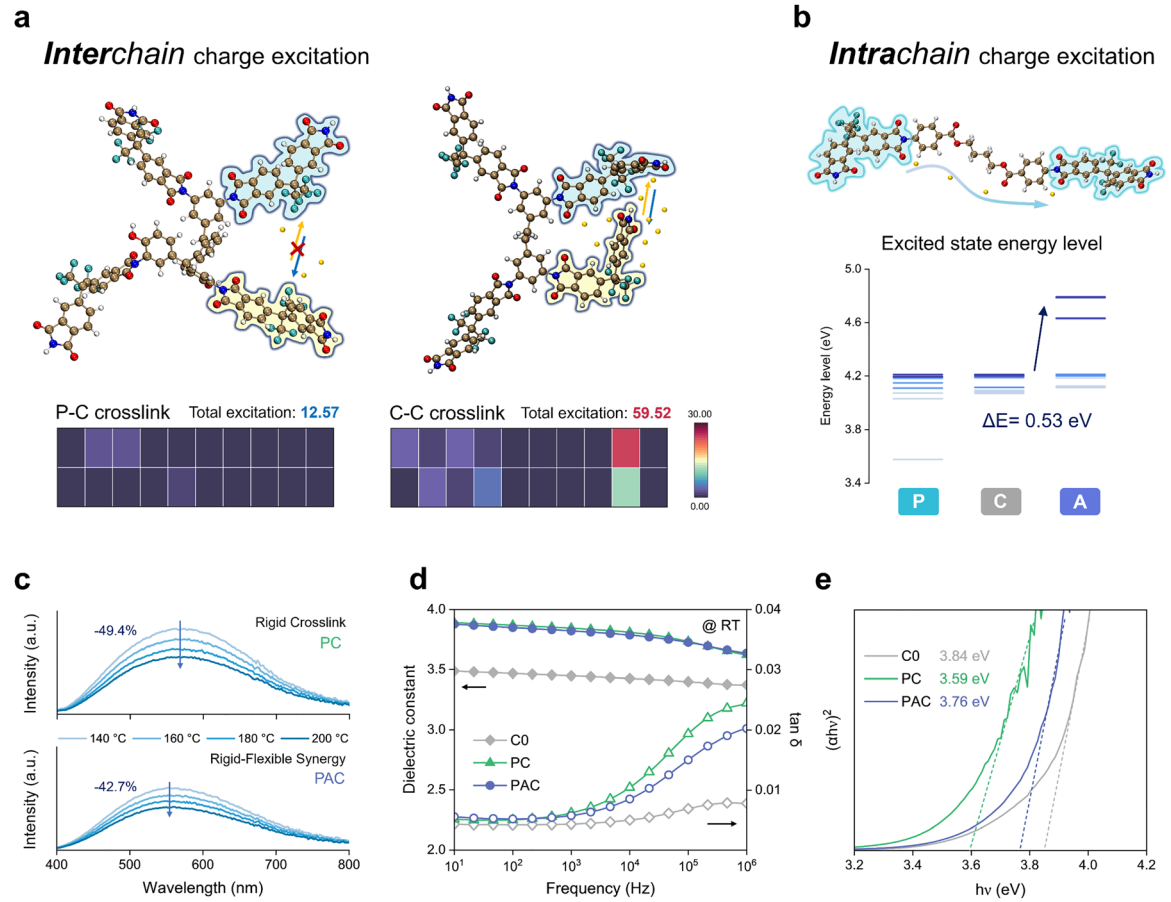

Fig. 2 Experimental investigations of charge transport suppression and dielectric response in crosslinked polymer systems. (a) Interchain charge excitation of P–C crosslink and C–C crosslink, (b) intrachain charge excitation of P, C and A unit characterized by electron transfer density matrix simulation. (c) Temperature-dependent fluorescence emission spectra of PC and PAC. (d) Dielectric constant and tan δ of C0, PC and PAC at room temperature. (e) Optimal bandgap results.

by the C unit, while the A unit (alkyl chain) demonstrates the highest barrier, with a 0.53 eV increase relative to the C unit. This trend supports that alkyl chain segments effectively hinder intrachain carrier transport by breaking π-conjugation pathways.

The above conclusions are corroborated by temperature-dependent fluorescence emission spectroscopy (Fig. 2c and Fig. S24). Fluorescence spectra of PC and PAC were acquired at temperatures ranging from 140 to 200 °C. Spectral shifts, whether blueshift or redshift, are frequently indicative of underlying structural modifications.[26–28] Interchain charge transfer induces fluorescence quenching (reduced intensity), and intrachain charge transfer is accompanied by fluorescence redshift.[29,30] For PC, the emission peak at 568 nm undergoes a 49.4% intensity decrease, indicative of thermally activated interchain carrier migration. In PAC, however, alkyl chain incorporation blue-shifts the peak to 556 nm and reduces the intensity decay to 42.7%. This attenuation stems from the synergistic effects of alkyl chains and phenolphthalein crosslinking: alkyl chains disrupt π-conjugation to elevate intrachain barriers; phenolphthalein rigidifies the network by enhancing interchain spacing and stabilizing chain conformations, along with alkyl chains homogenize chain packing distributions. Their combined action effectively suppresses interchain carrier transport through spatial confinement. Meanwhile, compared to alkyl side chains, the alkyl backbone demonstrates a more pronounced ability to suppress intra-chain charge carrier transport.

Fig. 2d illustrates the dielectric properties of the polymers. Uncrosslinked linear chains (C0) exhibit a dielectric constant (ε_r) of 3.5 and the lowest tan δ, indicating minimal relaxation losses due to unrestricted chain dynamics. Although such relaxation losses are not predominant under high-temperature energy storage conditions, the observed differences still reflect variations in the chain architecture and polarization behavior. Notably, PC and PAC display comparable ε_r values, as alkyl chains in PAC marginally enhance the polarization orientation capability of the polymer backbone despite their inherent low polarity nature. The tan δ further reveals that PAC exhibits significantly lower relaxation losses at a frequency above 10^3 Hz than PC, demonstrating the efficacy of the rigid-flexible synergistic design: local chain stabilization reduces segmental movement, while global conformational flexibility minimizes friction dissipation from large-scale chain motions.

The carrier transport behavior induced by aromatic conjugation in polymers is reflected in their optical bandgaps (Fig. 2e

and Fig. S25), where a higher bandgap indicates reduced electron delocalization and weakened π–π interactions. PC exhibits a lower bandgap (3.59 eV) compared to PAC (3.76 eV). This discrepancy arises from the distorted chain architecture in PC with rigid crosslinking alone, which likely induces localized dense packing in certain regions (as evidenced by WAXD/SAXS spatial heterogeneity) and enhances π-electron delocalization. In contrast, the alkyl chains in PAC homogenize chain packing and maintain a larger average interchain spacing of 6.30 Å, collectively suppressing interchain π–π coupling and delocalization pathways.

2.4. Dielectric behavior and localized carrier engineering

Temperature-dependent broadband dielectric spectroscopy (BDS) was employed to probe the dielectric response and molecular chain dynamics of the polymers across varying temperatures and frequencies (Fig. 3a–c and Fig. S26). In BDS spectra, relaxation peaks signify thermally activated dipole orientation processes. Below the peak temperature, increasing thermal energy facilitates dipole alignment, elevating the dielectric constant (ε_r). Beyond the peak, however, thermal agitation disrupts ordering, causing ε_r to decline. The peak temperature correlates with molecular chain segment mobility, reflecting a thermally governed relaxation mechanism.[31,32] As presented in Fig. 3a, the absence of side-chain crosslinking structures precludes the observation of significant chain relaxation in C0. Its ε_r increases slightly (from 3.34 to 3.47) below 100 °C and stabilizes thereafter, indicating that the main chain orientation of this linear chain structure is sufficiently thermally activated around 100 °C.

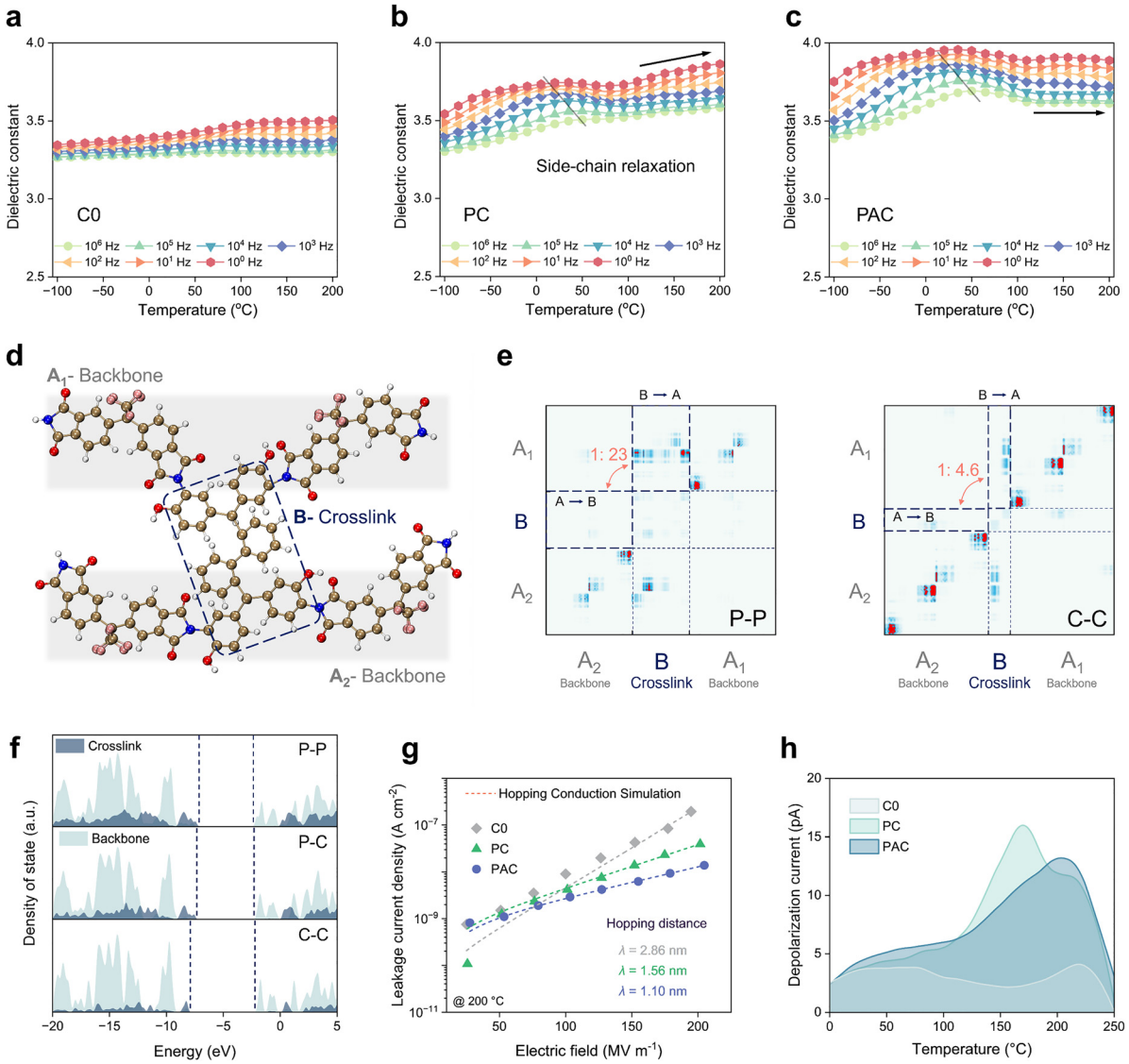

Fig. 3 Carrier confinement engineering and thermally activated charge transport in crosslinked polymer systems. (a)–(c) Temperature-dependent dielectric constant BDS results. (d) Structural illustration of the carrier excitation section of crosslink and main-chain (P–P as an example). (e) Total transfer amounts of electrons. (f) Density of states of P–P, P–C and C–C crosslinks and the backbone. (g) Leakage current results and hopping conduction simulation. (h) Thermally stimulated depolarization current of C0, PC and PAC.

The dielectric relaxation of the polymer comprises three distinct modes: end-to-end relaxation, segmental relaxation, and secondary relaxation.[33] End-to-end relaxation is only clearly observable in polymers with dipoles accumulated along the chain. In contrast, segmental relaxation arises from dipoles perpendicular to the chain, which exhibit a dominant contribution from segmental dynamics and show no dielectric response from chain modes. Secondary relaxation originates from the motion of side-chain dipoles. For polyimides with rigid imide rings in the main chain, both end-to-end and segmental relaxations are not prominent. Therefore, in the case of C0, which lacks side-chain crosslinking, the segmental relaxation behavior is not distinctly reflected in the BDS measurements. This observation is further supported by the temperature and frequency-dependent loss tangent spectra (Fig. S26).

PC (Fig. 3b) exhibits a low-frequency relaxation peak near 25 °C ($<10^4$ Hz) but is absent at higher frequencies (10^5–10^6 Hz), demonstrating suppressed high-frequency chain vibrations by rigid crosslinks. Because of the lack of glass transition below 300 °C (Fig. S15), this low-temperature relaxation originates from the thermally activated motion of the side chain. Notably, as the temperature rises to 200 °C, the ε_r of PC continues to increase, suggesting that local segmental motions at temperatures above side-chain mobility but below the main-chain movement temperature (T_g) are thermally activated. This behavior resembles an annealing behavior induced by the uneven chain distribution caused by rigid crosslinking.

In comparison, PAC exhibits distinct relaxation peaks across all frequencies, including 10^5 and 10^6 Hz, indicating a higher degree of thermal activation of polarization and disturbance in the side chains compared to PC, along with enhanced chain mobility (Fig. 3c). The unchanged relaxation peak positions relative to PC imply unaltered relaxation dynamics at crosslinked sites despite alkyl chain incorporation. Furthermore, the ε_r of PAC shows little variation with increasing temperature after the relaxation peak, indicating that its molecular chain structure has attained a thermodynamically equilibrated chain architecture. The statistical plots of the dielectric constant as a function of temperature for C0, PC, and PAC are presented in Fig. S27.

Electrostatic potential calculations of crosslinked structures (Fig. S28) demonstrate that phenolphthalein-based crosslinks exhibit a distinct reverse potential distribution relative to the main chain, contrasting with short-chain C–C crosslinks. This potential reversal drives the effect of complementary charge distribution between phenolphthalein and aromatic main chains that restrict π-electron delocalization, promoting carrier localization-a phenomenon supported by TDM analysis (Fig. 3d and e). Systematic TDM calculations reveal directional carrier transport dominance in P–P crosslinks, where crosslink-to-backbone (B → A) density exceeds the reverse (A → B) by 22.9-fold, indicating exceptional hole localization efficiency per crosslink site despite their low abundance (1%). In contrast, C–C crosslinks predominantly enable intra main-chain migration and show little localization (B → A/A → B = 4.64). Although P–C crosslinks (Fig. S29) exhibit weaker hole localization (B → A/A → B = 7.14) than P–P, they still surpass those of C–C systems. These findings highlight that phenolphthalein-derived crosslinks achieve superior carrier suppression through dual energy confinement (deep traps from potential inversion) and spatial restriction (larger migration pathways). Simultaneously, the density of states (DOS) with different structures also confirms this: the HOMO of the P–P and P–C crosslinking points (indicated by the left section of dark regions in Fig. 3f) is closer to the LUMO of the main chain (right section of light regions) than that of the C–C crosslinking points, indicating that they serve as deeper hole traps.[34,35]

The high-temperature insulating performance of the materials was evaluated through field-dependent leakage current density measurements. As shown in Fig. 3g and Fig. S30, C0 exhibits a significantly faster increase in leakage current density with electric field compared to PC and PAC, at 200 MV m^{-1}, the leakage current density of C0 reaches 1.94×10^{-7} A cm^{-2}, while PAC demonstrates a value one order of magnitude lower (1.38×10^{-8} A cm^{-2}). Fitting the leakage current data to the hopping conduction model[36] yields $R^2 > 0.99$, confirming hopping transport as the dominant mechanism. The hopping distance (λ), inversely correlated with trap depth, further reveals structural insights: C0, PC, and PAC exhibit λ values of 2.86 nm, 1.56 nm, and 1.10 nm, respectively. The reduced λ in PC originates from phenolphthalein crosslinks that localize holes through deep traps. PAC achieves a shorter hopping distance by eliminating the aggregated and distorted trapping sites inherent to PC, thereby enhancing carrier localization. The trend in trap depths was further corroborated by thermally stimulated depolarization current (TSDC) measurements, where higher depolarization peak temperatures correspond to deeper traps.[37] C0 exhibits a weak broad peak with negligible intensity (Fig. 3h). PC displays two peaks at 168 °C (dominant) and 205 °C, while PAC shows a single broad peak at 205 °C. This suggests that the 168 °C peak is related to the distorted and stacked phenolphthalein structures, whereas upon uniform chain distribution, the dispersed phenolphthalein crosslinks enhance carrier localization capacity, as indicated by T_{peak} = 205 °C.

2.5. Capacitive performances and stability

The breakdown strength distribution of the polymers, analyzed *via* Weibull statistical modeling (Fig. 4a and Fig. S31), demonstrates a correlation with leakage current density, consistent with electrical breakdown-dominated mechanisms. At 200 °C, C0, PC, and PAC exhibit progressively increased breakdown strengths of 485 MV m^{-1}, 546 MV m^{-1}, and 620 MV m^{-1}, respectively. Electrical tree propagation simulations (Fig. 4b) reveal the failure modes: the non-crosslinked and strongly conjugated structure of C0 exhibited the most pronounced electrical tree evolution and propagation. In contrast, the introduction of a crosslinked structure and the regulation of chain distribution enhanced charge carrier localization, effectively impeding the evolution of electrical trees and promoting energy dissipation during the evolution process.

Fig. 4c presents the capacitive performances of C0, PC and PAC at 200 °C and 100 Hz, which were deduced from the

unipolar electric displacement field loop approach (Fig. 4d and Fig. S32). Although C0 exhibits the lowest room-temperature tan δ (Fig. 2d), its tan δ under operational conditions is comparable to PC and PAC ($\sim$0.01, Fig. S26), and the rapidly increasing leakage current in C0 results in the highest energy loss and the lowest discharge energy density at equivalent fields, with the maximum discharged energy (U_d) $<$ 3 J cm^{-3}. In PC, heterogeneously distributed phenolphthalein crosslinks partially suppress interchain conjugation and form carrier localization structures, reducing energy loss while maintaining $>$90% efficiency at 550 MV m^{-1} breakdown. PAC demonstrates superior high-temperature insulation and carrier confinement due to its flexible segments that effectively mitigate defects induced by excessive rigidity, and it achieves the lowest energy loss and highest breakdown resistance (650 MV m^{-1}), delivering a U_d of 6.91 J cm^{-3} with high efficiency.

For dielectric polymers, excessive energy loss (as waste heat) at low charge–discharge efficiency can elevate system temperature, degrading insulation, exacerbating energy loss and likely forming a vicious cycle.[38] Thus, we focus on discharge energy density under high-efficiency conditions.[39] As summarized in Fig. 4e, PAC achieves an average maximum U_d of 5.05 J cm^{-3} at 95% efficiency, outperforming other materials, which is even higher than their U_d at 90% efficiency. Fig. 4f presents the performances of recent outstanding works in energy storage at 200 °C, demonstrating U_d at 90% charge–discharge efficiency, with PAC also achieving a commendable level within this context.[14,40–46]

The rapid charge–discharge capability is a crucial characteristic that distinguishes electrostatic capacitors from other energy storage devices. We characterized the discharge rate of PAC through rapid discharge tests based on load resistance (see Fig. 4g). Under a load resistance of 100 kΩ, PAC exhibited a 95% discharge time ($\tau_{0.95}$) of 5.87 μs at 200 °C, which is superior to the $\tau_{0.95}$ of 7.44 μs for the state-of-the-art commercial material BOPP at 120 °C, indicating its promising rapid discharge

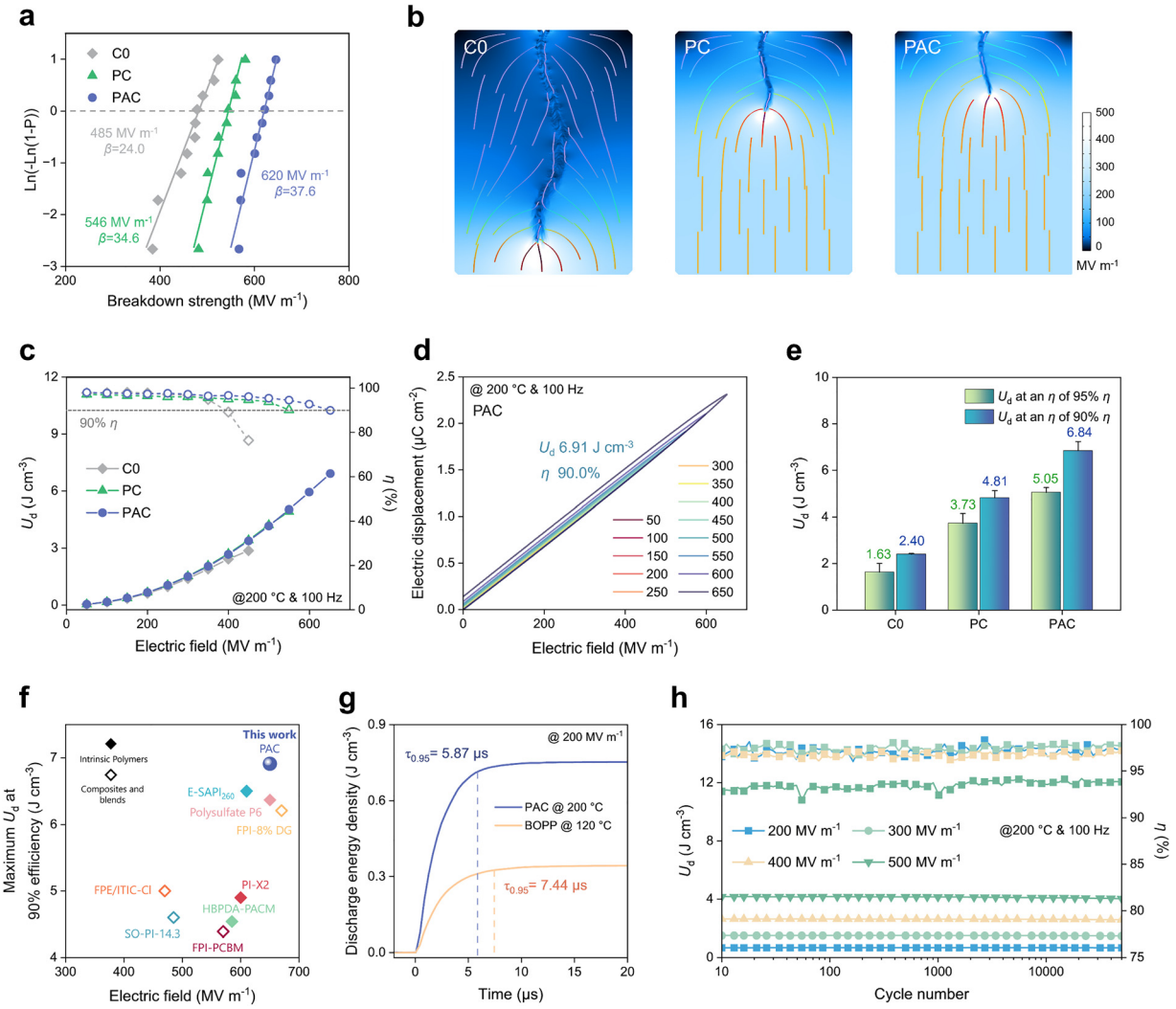

Fig. 4 Capacitive performances and stability of polymers. (a) Breakdown strengths and (b) electrical tree propagation simulations of C0, PC and PAC. (c) Capacitive performances of polymers at 200 °C & 100 Hz. (d) *P*–*E* loops of PAC. (e) Average maximum U_d at high efficiency of polymers. (f) Comparison of the energy storage performance at 200 °C and 90% efficiency. (g) Rapid discharge tests, with the load resistance (R_L) of 100 kΩ. (h) Cycling stability of PAC.

capability. Furthermore, PAC also shows decent cycling stability (Fig. 4h). After 50 000 charge–discharge cycles at 200–500 MV m^{-1}, its U_d and efficiency remain highly stable, retaining over 93% efficiency and a U_d about 4.1 J cm^{-3} at 500 MV m^{-1}. Meanwhile, large-area, uniform PAC films can also be obtained *via* solution casting (Fig. S33).

3. Conclusions

In summary, we propose a rigid–flexible synergistic multiple crosslinked network strategy that simultaneously suppresses interchain and intrachain charge transport while reducing molecular chain thermal motion, achieving exceptional high-temperature energy storage performance. Rigid crosslinking enhances conformational stability and increases interchain spacing to inhibit chain conjugation and thermal agitation, while flexible motifs mitigate chain packing heterogeneity induced by excessive rigidity. The rigid–flexible synergy yields homogeneous chain distribution and reduced interchain/intrachain charge transfer. Additionally, phenolphthalein crosslinks exhibit a reverse electrostatic potential relative to the main chain, amplifying carrier localization and high-temperature insulation. PAC demonstrates the lowest leakage current density and highest breakdown strength (620 MV m^{-1}), delivering an energy density of 6.91 J cm^{-3} at 200 °C with 90% efficiency. Its rapid discharge capability and cycling stability further validate the efficacy of this strategy. These results highlight the potential of rigid–flexible synergistic crosslinking for promoting superior high-temperature energy storage performance for all-polymer dielectrics.

Conflicts of interest

The authors declare no conflict of interest.

Data availability

The data supporting this article have been included as part of the supplementary information (SI). Supplementary information is available. See DOI: https://doi.org/10.1039/d5ee04064g.

Acknowledgements

The authors acknowledge financial support from the Jiangmen Science and Technology Plan Project (2023780200090009181).

References

1 J. Chen, Y. Zhou, X. Huang, C. Yu, D. Han, A. Wang, Y. Zhu, K. Shi, Q. Kang, P. Li, P. Jiang, X. Qian, H. Bao, S. Li, G. Wu, X. Zhu and Q. Wang, *Nature*, 2023, **615**, 62–66.
2 M. Yang, H. Li, J. Wang, W. Shi, Q. Zhang, H. Xing, W. Ren, B. Sun, M. Guo, E. Xu, N. Sun, L. Zhou, Y. Xiao, M. Zhang, Z. Li, J. Pan, J. Jiang, Z. Shen, X. Li, L. Gu, C. Nan, X. Wang and Y. Shen, *Nat. Energy*, 2024, **9**, 143–153.
3 Q. Li, L. Chen, M. Gadinski, S. Zhang, G. Zhang, H. Li, E. Iagodkine, A. Haque, L. Chen, T. Jackson and Q. Wang, *Nature*, 2015, **523**, 576.
4 Z. Zhang, D. Wang, M. Litt and L. T. L. Zhu, *Angew. Chem., Int. Ed.*, 2018, **57**, 1528.
5 L. Li, W. Xu, G. Rui, S. Zhang, Q. Zhang and Q. Wang, *Chem. Sci.*, 2024, **15**, 19651.
6 J. Hao, I. Mutegi, M. Mukherjee, H. Sahu, A. Khomane, M. Yassin, R. Ramprasad, G. Sotzing and Y. Cao, *Proc. Natl. Acad. Sci. U. S. A.*, 2024, **121**, e2415388121.
7 Z. Xie, L. Fan, H. Li, Z. Ran, S. Lai, X. Liu, A. Deatherage, Y. Wang, Q. Li, Y. Yin and Y. Liu, *Prog. Polym. Sci.*, 2025, **164**, 101957.
8 J. Pei, J. Zhu, L. Yin, Y. Zhao, M. Yang, S. Zhong, Q. Feng and Z. Dang, *Adv. Funct. Mater.*, 2024, **34**, 2316869.
9 X. Li, P. Hu, J. Jiang, J. Pan, C. Nan and Y. Shen, *Adv. Mater.*, 2025, **37**, 2411507.
10 W. Zhang, D. Ai, S. Fan, R. Yang, X. Du, X. Yang, F. Lv, Y. Liu, Y. Cheng and X. Yu, *Energy Storage Mater.*, 2025, **77**, 104180.
11 H. Li, B. S. Chang, H. Kim, Z. Xie, A. Laine, L. Ma, T. Xu, C. Yang, J. Kwon, S. Shelton, L. Klivansky, V. Altoe, B. Gao, A. Schwartzberg, Z. Peng, R. Ritchie, T. Xu, M. Salmeron, R. Ruiz, K. Sharpless, P. Wu and Y. Liu, *Joule*, 2023, **7**, 95–111.
12 Q. Xie, W. Liao, W. Gong, C. Huang, S. Huang and Q. Zhang, *Nano Lett.*, 2025, **25**, 7793–7800.
13 R. Wang, Y. Zhu, S. Huang, J. Fu, Y. Zhou, M. Li, L. Meng, X. Zhang, J. Liang, Z. Ran, M. Yang, J. Li, X. Dong, J. Hu, J. He and Q. Li, *Nat. Mater.*, 2025, **24**, 1074–1081.
14 G. He, H. Luo, Y. Liu, Y. Wan, B. Peng, D. Hu, F. Wang, X. Li, J. Peng, H. Wang and D. Zhang, *Energy Environ. Sci.*, 2025, **18**, 2405–2414.
15 B. Wang, J. Zou, B. Liu, Z. Wang, B. Li, D. Xu, Q. Li and S. Luan, *Mater. Horiz.*, 2025, **12**, 4841–4850.
16 M. Yang, L. Zhou, X. Li, W. Ren and Y. Shen, *Adv. Mater.*, 2023, **35**, 2302392.
17 Z. Pan, L. Li, L. Wang, G. Luo, X. Xu, F. Jin, J. Dong, Y. Niu, L. Sun, C. Guo, W. Zhang, Q. Wang and H. Wang, *Adv. Mater.*, 2023, **35**, 2207580.
18 C. Qian, R. Bei, T. Zhu, W. Zheng, S. Liu, Z. Chi, M. Aldred, X. Chen, Y. Zhang and J. Xu, *Macromolecules*, 2019, **52**, 4601–4609.
19 A. Papon, K. Saalwachter, K. Schaler, L. Guy, F. Lequeux and H. Montes, *Macromolecules*, 2011, **44**, 913–922.
20 V. Litvinov, R. Orza, M. Kluppel, M. Duin and P. Magusin, *Macromolecules*, 2011, **44**, 4887–4900.
21 Z. Ran, R. Wang, J. Fu, M. Yang, M. Li, J. Hu, J. He and Q. Li, *Adv. Mater.*, 2023, **35**, 2303849.
22 X. Dong, Y. Wang, Y. Cao, N. Li, J. Fu, Y. Wang, J. Yu and Z. Hu, *Chem. Eng. J.*, 2024, **15**, 157312.
23 R. Singh, M. Pai, A. Banerjee, A. Shrivastava, U. Kumar, I. Sinha, B. Dutta, P. Hassan, R. Ningthoujam, R. Ghosh, S. Nath, R. Sharma, Jagannath and R. Bapat, *ACS Omega*, 2024, **9**, 40182–40203.
24 B. Vincent Crist, *J. Vac. Sci. Technol., A*, 2024, **42**, 032803.

25 W. Sima, Y. Mai, P. Sun, M. Yang, T. Yuan, B. Chen and Y. Yang, *Energy Storage Mater.*, 2025, **74**, 103974.
26 J. Park, S. Kim, W. Kim, Z. Sun, B. Lee and C. Yang, *Energy Environ. Sci.*, 2025, **18**, 6260–6272.
27 Y. Cho, D. Koo, H. Nho, J. Park, S. Yang, Y. Kim, S. Jeong, Z. Sun, G. Jeong, E. Son, O. Kwon, H. Park and C. Yang, *Energy Environ. Sci.*, 2025, **18**, 8161–8170.
28 Y. Cho, Z. Sun, G. Li, D. Zhang, S. Yang, T. Marks, C. Yang and A. Facchetti, *J. Am. Chem. Soc.*, 2025, **147**, 758–769.
29 Y. Xin, Y. Zhu, R. Chi, C. Duan, P. Yan, C. Han and H. Xu, *Adv. Mater.*, 2023, **25**, 2304103.
30 I. Azumaya, H. Kagechika, Y. Fujiwara, M. Itoh, K. Yamaguchi and K. Shudo, *J. Am. Chem. Soc.*, 1991, **113**, 2833–2838.
31 S. Bonardd, A. Alegria, C. Saldias, A. Leiva and G. Kortaberria, *Polymer*, 2020, **203**, 122765.
32 S. Bonardd, A. Alegria, O. Ramirez, C. Saldia, A. Leiva and G. Kortaberria, *React. Funct. Polym.*, 2019, **140**, 1–13.
33 I. Popov, S. Cheng and A. Sokolov, Broadband Dielectric Spectroscopy and Its Application in Polymeric Materials. In Macromolecular Engineering.
34 J. Zha, M. Xiao, B. Wan, X. Wang, Z. Dang and G. Chen, *Prog. Polym. Sci.*, 2023, **140**, 101208.
35 Z. Meng, T. Zhang, C. Zhang, Y. Shang, Q. lei and Q. Chi, *Adv. Mater.*, 2024, **36**, 2310272.
36 R. Wang, Y. Zhu, J. Fu, M. Yang, Z. Ran, J. Li, M. Li, J. Hu, J. He and Q. Li, *Nat. Commun.*, 2023, **14**, 2406.
37 Y. Zhou, C. Yuan, S. Wang, Y. Zhu, S. Cheng, X. Yang, Y. Yang, J. Hu, J. He and Q. Li, *Energy Storage Mater.*, 2020, **28**, 255–263.
38 M. Yang, M. Guo, E. Xu, W. Ren, D. Wang, S. Li, S. Zhang, C. Nan and Y. Shen, *Nat. Nanotechnol.*, 2024, **19**, 588–603.
39 B. Sun, J. Zou, W. Qiu, S. Tian, M. Wang, H. Tang, B. Wang, S. Luan, X. Tang, M. Wang and D. Ma, *Natl. Sci. Rev.*, 2025, **12**, nwae393.
40 J. Dong, L. Li, Y. Niu, Z. Pan, Y. Pan, L. Sun, L. Tan, Y. Liu, X. Xu, X. Guo, Q. Wang and H. Wang, *Adv. Energy Mater.*, 2024, **14**, 2303732.
41 Z. Ran, M. Yang, R. Wang, J. Li, M. Li, L. Meng, Y. Liu, J. Hu, J. He and Q. Li, *Energy Storage Mater.*, 2025, **74**, 103952.
42 W. Huang, B. Wan, X. Yang, M. Cheng, Y. Zhang, Y. Li, C. Wu, Z. Dang and J. Zha, *Adv. Mater.*, 2024, **36**, 2410927.
43 Y. Zhou, Y. Zhu, W. Xu and Q. Wang, *Adv. Energy Mater.*, 2023, **13**, 2203961.
44 M. Yang, W. Ren, Z. Jin, E. Xu and Y. Shen, *Nat. Commun.*, 2024, **15**, 8647.
45 H. Li, H. Zheng, T. Yue, Z. Xie, S. Yu, J. Zhou, T. Kapri, Y. Wang, Z. Cao, H. Zhao, A. Kemelbay, J. He, G. Zhang, P. Pieters, E. Dailing, J. Cappiello, M. Salmeron, X. Gu, T. Xu, P. Wu, Y. Li, K. Sharpless and Y. Liu, *Nat. Energy*, 2025, **10**, 90–100.
46 W. Ren, M. Yang, L. Zhou, Y. Fan, S. He, J. Pan, T. Tang, Y. Xiao, C. Nan and Y. Shen, *Adv. Mater.*, 2022, **23**, 2207421.